Xe and Ar nanobubbles in Al studied by photoemission spectroscopy

R. S. Dhaka, C. Biswas, A. K. Shukla, and S. R. Barman*
UGC-DAE Consortium for Scientific Research, Khandwa Road, Indore 452001, Madhya Pradesh, India

Aparna Chakrabarti
Raja Ramanna Centre for Advanced Technology, Indore 452013, Madhya Pradesh, India

(Received 18 October 2007; revised manuscript received 26 December 2007; published 25 March 2008)

We have studied xenon and argon bubbles formed in the subsurface region of Al(111) by x-ray photoelectron spectroscopy. As a consequence of the nanometer size of the bubbles, the photohole formed by Xe $3d$ or Ar $2p$ photoemission is screened by the Al conduction electrons, which substantially lowers the binding energy (BE) as compared to the gas phase. As the bubble size increases, the Al conduction electron screening decreases and the BE increases. On the basis of density functional theory, we show that the change in the bubble pressure with size is not responsible for the BE shift of inner shell core levels, such as Xe $3d$ or Ar $2p$. On the other hand, an increase in BE with bubble size for outer shell core levels, such as Ar $3p$, could be due to a decrease in both pressure and Al conduction electron screening. The core level line shape also changes with bubble size. For example, the spectra are broadened due to the distribution of the bubble radius around its mean value, and an asymmetry for small bubbles is observed that decreases for larger bubbles. An annealing of Xe and Ar bubbles after an implantation up to 640 K shows that the BE increases with annealing temperature. Since it is well known that bubble size increases with annealing temperature, this further supports our contention of BE shift with bubble size. A defect induced partial disorder of the Al(111) surface by Xe and Ar bombardment is observed by low energy electron diffraction, but this does not affect the Al $2p$ BE and line shape.

DOI: 10.1103/PhysRevB.77.104119 PACS number(s): 82.80.Pv, 61.80.Jh, 79.60.−i

I. INTRODUCTION

The formation of rare gas (rg) bubbles in Al is a well known phenomenon and has been a topic of extensive research.[1–8] The reasons for interest in rg bubbles arise from the different interesting physical phenomena they exhibit. For example, the bubbles can be in solid state even at room temperature, they are overpressurized, form at high mass densities, and can be superheated.[3,4] Besides, an electron interference between subsurface rg bubbles and the Al surface has been reported.[5] Studying the rg bubbles is technologically importance in the context of fission reactors, integrated circuits, ion beam milling of layered structures, and sputter growth of thin films.[9,10]

The implanted rg atoms in the nearly free electron metals, such as Al, with sizable conduction electron density precipitate into bubbles because of the repulsive pseudopotential and negative heat of solution. This makes rg atoms in Al insoluble and it is energetically favorable for them to form bubbles.[11] Schmid *et al.*[5] found a correlation between the number of bubbles and the amount of implanted Ar. Many different experimental and theoretical studies[1,3–8,11] show that most of the implanted Xe or Ar atoms equilibrate into bubbles with a symmetric size distribution. The bubble sizes have been estimated by different groups. For example, for Ar bubbles in Al using transmission electron microscopy (TEM), the bubble radius (R) is estimated to be 13.5–15 Å.[1,4] R for different rg atoms (from He to Xe) in Al has been reported to be in the range of 6.5–20 Å, depending on the implantation conditions.[1]

The isolated rg atoms implanted in a metal constitute a simple model system to study the interaction between an inert foreign atom and the metal host. Studies have been performed in the past to understand the origin of core level binding energy (BE) shifts between the gas phase and the implanted rg atoms.[12–15] Citrin and Hamann observed a 2–4 eV decrease in BE of the rg core levels in the metal host with respect to the gas phase. Waclawski *et al.*[11] used ultraviolet (UV) photoelectron spectroscopy measurements for a rg implanted in Ge and observed the shift in peak position with respect to the gas phase.[14] The implantation results in compression of the wave functions of its outer electrons. Thus, the core electron BE is reduced because the Coulomb interaction between the outer and core electrons is increased.[13] Physisorbed rg layers on a single crystal metal surface are ordered and have been studied by using both x-ray photoemission spectroscopy (XPS) and angle resolved photoemission.[16,17] However, studies on rg bubbles in Al implanted at low incident ion energies are very few in literature.[8] This is primarily because, in most of the studies, a high implantation energy (E_i) in the range of 30–50 keV has been used. The penetration depth of a rg in such a case is in the micron range, which is larger than the maximum probing depth of photoemission, what is about 50 Å from the surface. The other difficulty is that even if bubbles could be formed in the subsurface region on a clean Al surface, an exposure to ambient conditions would immediately oxidize the surface.

In our earlier study, we carried out *in situ* XPS investigation of Ar bubbles formed in the subsurface region of Al(111).[8] In this paper, we have studied Xe bubbles in Al(111) by photoemission spectroscopy and have compared the results with those of Ar bubbles. A higher E_i of up to 5 keV has been used here as compared to our previous work.[8] We found that BE increases with E_i due to the increase in bubble size. An increase in bubble size decreases the Al conduction electron screening. The asymmetry of core level line shape decreases with increasing bubble size. Based on density functional calculations, we discard the explana-

tion that a change in pressure can cause a BE shift in the inner shell core levels, such as Ar $2p$ or Xe $3d$. On the other hand, for Ar $3p$, which is an outer shell core level, a pressure change could influence the BE. The overall similarity of the behavior of Xe and Ar core levels establishes a general trend that should be valid for any inert gas nanobubble in Al.

II. EXPERIMENTAL METHOD

A commercial electron energy analyzer from Specs GmbH, Berlin, has been used to perform the XPS measurements at 4×10^{-11} mbar base pressure. The energy resolution was 0.8 eV with the pass energy set at 20 eV, and a slit size of 6 mm diameter was used in a medium magnification mode. An Al(111) single crystal was cleaned by repeated cycles of sputtering by using 1–2 keV Ar^+ ions and subsequent annealing at 723 K to regenerate surface order, which is characterized by a sharp (1×1) low energy electron diffraction (LEED) pattern, as shown later in Fig. 10(a). The annealing at 723 K also removes any implanted rg during sputtering and this is checked by recording the rg core level regions before and after sputtering and annealing. Before each implantation, it was ensured that the carbon and oxygen contaminations are in the noise level. Xe and Ar ions were bombarded *in situ* in normal incidence geometry at a pressure of $(1-2)\times10^{-5}$ mbar for different durations with a substrate temperature of about 340 ± 10 K. For each E_i and fluence combination, we have implanted the rg on a clean Al(111), and not additively on an already implanted Al surface. For example, to reach a 3 monolayer (ML) fluence, we do not implant 1 ML rg on the Al surface previously implanted with 2 ML rg; rather, we implant 3 ML continuously on a clean Al surface.

The fluence (F) is given in units of monolayer. A fluence of 1 ML means that 1.415×10^{15} rg atoms/cm^2 [the number of atoms on the Al(111) surface] have been bombarded on the Al surface. F is calculated by the following expression:

$$F=\frac{Qt}{A(1.415\times10^{15})}, \tag{1}$$

where Q is the total charge flowing through the sample per unit time, which is calculated by measuring the sample current, and t is the time for which the ion beam is incident on the sample. A is the area of the sample exposed to the ion beam, which is determined from the geometry of the experiment and the full width at half maximum (FWHM) of the ion beam, which depends on the distance between the ion gun and the sample.

The Ar $2p$ core level spectra were fitted with two Doniach–Šunjić (DS) line shapes[18] corresponding to the two spin-orbit components of Ar $2p$, using a least-square error minimization routine based on the Levenberg–Marquardt algorithm.[19] The DS line shape is characterized by parameters such as its position, intensity, intrinsic lifetime broadening (γ), and the asymmetry parameter (α). α and γ have been taken to be same for both spin-orbit components. In the case of α, in order to avoid unphysical values and resulting problems with the convergence of the fitting routine, we constrained it to be greater than or equal to zero. In the case of γ, we noted that its minimum value is the intrinsic lifetime determined with high resolution studies for a gas phase. This value is 0.059 and 0.25 eV for Ar $2p$ and Xe $3d_{5/2}$, respectively.[20] In order to account for the instrumental factors (i.e., the analyzer and the photon source related broadenings), the DS line shape has been convoluted with a Voigt function. This Voigt function can be regarded as characteristic of the instrument and is dependent on photon source and analyzer settings for the measurements. The parameters defining the Voigt function (for example, the Lorentzian and Gaussian broadenings) have been obtained from a fitting of the Al $2p$ core level spectrum of a clean Al(111), for which the intrinsic lifetime broadening and α are well known.[21,22] The Xe $3d$ and Ar $2p$ spectra have been collected with the same analyzer settings and, hence, the same broadening parameters as determined for a clean Al $2p$ were used to convolute the rg DS line shape. However, it was observed that if the instrumental Lorentzian and Gaussian broadening parameters were allowed to vary, the Gaussian parameter quite substantially increased from the instrumental value. Hence, from the fitting, it was clear that besides the DS line shape and instrumental broadening, a further Gaussian broadening of the rg core level spectra is required. So, an additional Gaussian broadening was used over and above the instrumental broadening. The FWHM of this Gaussian (w_g) was also varied. The residual for the fitting is within the statistical scatter of the experimental data. In our fitting scheme for Ar $2p$, the spin-orbit splitting and the branching ratio have been freely varied, and we obtain a spin-orbit splitting of 2.1 ± 0.1 eV with a branching ratio of 1.9 ± 0.1.

III. RESULTS AND DISCUSSION

A. Binding energy shift with implantation energy

The Xe $3d_{5/2}$ core level spectra for 1 ML fluence of Xe bubbles in Al(111) are shown in Fig. 1 for different E_i. For comparison, a spectrum is recorded in the same energy range after exposing the Al surface to 1000 L (1 L$=10^{-6}$ Torr s) of Xe at room temperature (bottom spectrum in Fig. 1). Xe signal is not observed. This is expected because Xe is not physisorbed on Al at room temperature. [17] Similarly, for an Ar exposed Al surface, we do not observe any signature of physisorption at room temperature.[8] Thus, the presence of a finite Xe $3d_{5/2}$ (or Ar $2p$) core level photoelectron peak after implantation indicates that the rg atoms reside in the subsurface region of Al.

From Fig. 1, for $E_i=0.2$ keV, the Xe $3d_{5/2}$ peak is at 669.95 ± 0.05 eV. This value is 2.25 eV smaller than the BE of Xe $3d_{5/2}$ in the gas phase, the gas phase BE being 672.2 eV (Al work function is 4.2 eV).[23] This comparison is done by taking the BE of Xe bubbles in Al and that of Xe in the gas phase with respect to the vacuum level of Al(111). Ar bubbles also exhibit a shift of 2.29 eV with respect to the gas phase.[8] From previous theoretical studies on implanted rg atoms in metals, the decrease in BE with respect to the gas phase was related to the relaxation shift.[12–14] This arises because of the extra atomic screening of the rg core hole by host metal conduction electrons in the photoemission final state and will be discussed in detail later. The extra atomic

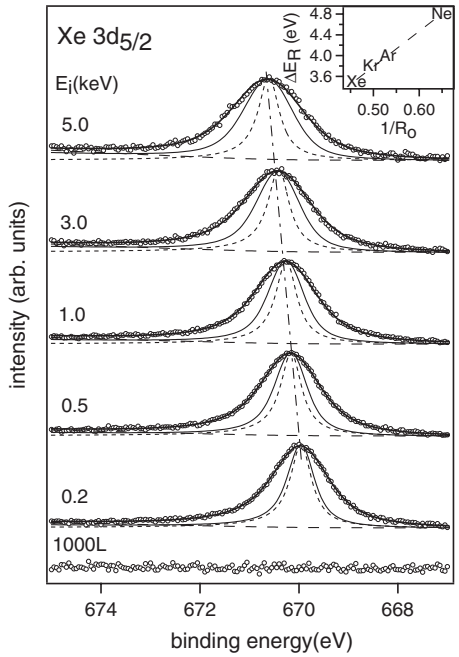

FIG. 1. Xe $3d_{5/2}$ core-level spectra (open circles) and the fitted curve (thick solid line) as a function of E_i for 1 ML fluence. The experimental spectra have been normalized to the same height. The deconvoluted DS line shape (short dashes), the spectral line shape including the Gaussian broadening but excluding the instrumental broadening (thin solid line), and the inelastic Tougaard background (long dashes) are shown below each spectrum. The spectrum for 1000 L Xe dosed Al(111) is shown at the bottom. The spectra are staggered along the vertical axis for clarity of presentation. The change in BE is indicated by a dot-dashed line. The inset shows a linear variation of the extra atomic screening for different rg atoms with inverse atomic radius (dashed line).

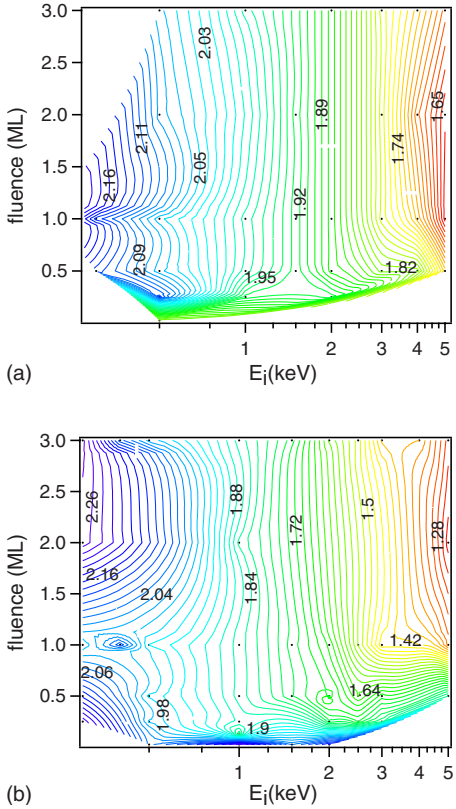

FIG. 2. (Color online) Contour plot showing the variation of ΔE_B (see text for definition) for (a) Xe $3d_{5/2}$ [in gray scale (rainbow for color): the darkest (blue) contour, 2.25 eV; the lightest (red) contour, 1.65 eV] and (b) Ar $2p$ [in gray scale (rainbow for color): the darkest (blue) contour, 2.29 eV; the lightest (red) contour, 1.3 eV] as a function of E_i and fluence. The dots represent the different E_i and fluence combinations where the experiments have been performed.

relaxation due to the other rg atoms in the bubble is also more efficient because of the large pressure exerted by the Al lattice. This even causes a change in the physical state of the bubble; for example, both Xe and Ar bubbles in Al are known to be in solid state at room temperature.[2]

It is interesting to note that Xe $3d_{5/2}$ BE gradually increases, with E_i varying from 0.2 to 5 keV (Fig. 1). Also, for other fluences ranging from 0.025 to 3 ML, an increase in BE with E_i has been observed. The spin-orbit split Xe $3d_{3/2}$ peak (not shown in Fig. 1) also exhibits a similar trend. In order to depict the variation of Xe $3d_{5/2}$ BE as a function of E_i and fluence, we define ΔE_B to be the BE of Xe $3d_{5/2}$ in the gas phase minus the BE of Xe $3d_{5/2}$ in the bubbles, as in Ref. 8. Thus, a smaller ΔE_B means a larger BE and ΔE_B=0 corresponds to the gas phase BE. Figure 2(a) shows the ΔE_B variation as a function of E_i and fluence in a contour plot. The spectra have been recorded for different E_i (0.2–5 keV) and fluence (0.025–3 ML) combinations, as shown by the dots in Fig. 2(a).

We found that for implantation conditions with small E_i and fluence, ΔE_B is large (2.25 eV), as shown by the color contours from blue to green. On the contrary, when E_i is large, ΔE_B is small (1.65 eV), as shown by the color contours from yellow to red. The overall variation, i.e., the difference between the smallest and the largest ΔE_B in the studied E_i and fluence range is about 0.6 eV. Except for some subtle difference, the ΔE_B variation for Xe $3d_{5/2}$ [Fig. 2(a)] is very similar to Ar $2p$ [Fig. 2(b)]. However, the maximum ΔE_B for Ar $2p$ is found to be slightly more (2.29 eV) than Xe $3d$ (2.25 eV). The overall variation of ΔE_B for Ar $2p$ is about 1.1 eV, which is substantially higher than that for Xe $3d$ (0.6 eV). This is also higher than that reported in Ref. 8 because here an E_i up to 5 keV is used in comparison to the 3 keV previously used.[8]

We first discuss the reason for the decrease in BE as compared to the gas phase (i.e., positive ΔE_B) of a rg when implanted in Al. This will also enable us to understand the variation of ΔE_B with E_i for the rg bubbles. A BE change in isolated rg atoms implanted in metals has been theoretically studied earlier.[12–14] There are two factors responsible for the BE shift. The first factor is the relaxation shift, ΔE_R, which is associated with the extra atomic screening of the core hole generated in the final state of photoemission by the metal conduction electrons. There is also a contribution from the intra-atomic screening due to a relaxation of the rg atom wave functions around the core hole. The second factor is the electrostatic shift that arises because, in the initial state, the

rg atom in the metal experiences a different potential as compared to the rg atom in the gas phase. This is due to the formation of dipole barriers at the bubble-Al interface, an increase in the Coulomb interaction between the valence and the core electrons due to compression, the physical state of the rg in the bubbles, etc.

Waclawski *et al.*[14] performed UV photoemission experiments on different rare gases implanted in Ge and estimated the extra atomic screening ΔE_R by using a linear dielectric response theory. They found, to a first approximation, that ΔE_R is inversely proportional to the radius of the cavity in which the rg is implanted. An extra atomic screening by conduction electrons, as estimated in Ref. 13 for different rg's, when plotted as a function of their inverse radius, shows a linear behavior (inset of Fig. 1). By using a density functional method, Citrin and Hamann[12] showed that ΔE_B for isolated rg atoms implanted in Cu, Ag, or Au is inversely proportional to the effective radius of the atoms. The physics of implanted rg atoms in metals can be carried over to rg bubbles in Al because of their nanometer size and because the Al conduction electron screening would be insignificant for large bubbles. On the other hand, the other causes of BE shift, such as intra-atomic screening, electrostatic shifts, or physical state, would not depend on the radius of the rg bubble.[8] Based on the above discussion, since the majority of the implanted rg's equilibrate into bubbles of nearly spherical shape, it can be argued that ΔE_B is inversely proportional to the effective radius of the bubble (R), which is given by

$$\Delta E_B = \Delta E_R + c_2 = \frac{c_1}{R} + c_2, \tag{2}$$

where c_1 is the proportionality constant and c_2 represents contributions to ΔE_B that are independent of R. Thus, the BE variation for the rg could be explained by the ΔE_R variation if the bubble size changes with implantation conditions. We experimentally found that ΔE_B varies with E_i; so the important question now is how or whether the bubble radius depends on E_i.

To answer the above question, first we discuss the different mechanisms of bubble formation. These are vacancy absorption, coalescence, and emission of dislocation loops.[24] In the very early stages, bubble growth occurs by a coalescence of an implanted rg atom with other rg atoms and the associated vacancies that allow them to diffuse. As the bubble size increases, to maintain the equilibrium pressure of $2\gamma/R$ (γ is the surface tension of the bubble), extra vacancies are required, which may be obtained by vacancy diffusion or by plastic deformation of the surrounding matrix. The latter results in the phenomenon of emission of dislocation loops, which is energetically favorable only when the pressure exceeds a threshold value.[24] However, for Xe and Ar, the pressure is less than the threshold value, as shown in Table III of Ref. 1. Thus, vacancy absorption and coalescence are the main mechanisms of bubble growth in the present case. Since a small E_i is used, the projected range or the implantation depth (d) is small and the bubbles are formed in the subsurface region. It should be noted that the rg ions in Al undergo diffusion after implantation. If d is large, the probability of rg atoms to backscatter out of the Al surface will be less, since more diffusion steps would be required for the rg atom to reach the surface and desorb.[25] Thus, for a larger d, the probability that rg atoms would coalesce to form bubbles would increase.

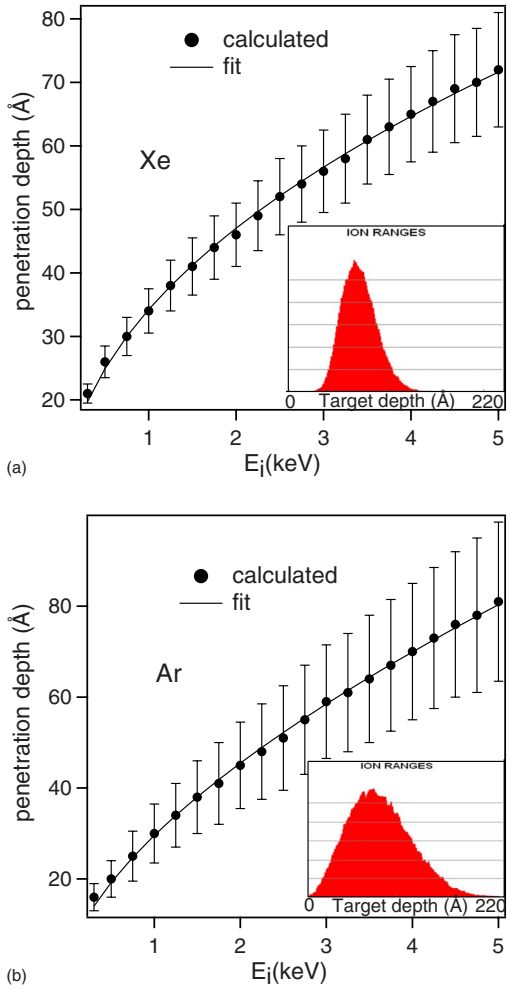

FIG. 3. (Color online) The calculated penetration depth (d) for (a) Xe and (b) Ar in Al as a function of E_i (filled circles). The fitted curve is shown as a solid line. The bars on each data point show the straggle. Insets show the ion distribution at 5 keV.

In order to find the variation of d with E_i, we have performed Monte Carlo calculations using the TRIM-2000 (Transport of Ions through Matter) code.[26,27] The calculation has been done using a full quantum mechanical treatment of ion-atom collisions for 50 000 ions incident with energy E_i at normal incidence geometry on the Al substrate. Xe exhibits a sharply peaked depth distribution [inset of Fig. 3(a)] with a FWHM of about 48 Å. For Ar, the width of the distribution is almost doubled (FWHM=97 Å), which indicates a higher diffusion for the lighter ion. The peak position of the depth distribution gives d, which increases with E_i in both cases (Fig. 3). d increases from 21 to 72 Å for Xe and from 16 to 81 Å for Ar in the studied ion energy range. The straggle, i.e., the width of the distribution about the peak of the projected range (shown by bars in Fig. 3 and by the FWHM of the distribution in the inset), increases with ion incidence energy. Martan has shown that an analytical ex-

pression can be used to relate d to E_i, where a leading term has a square root dependence on E_i.[28] Based on this, we used an expression $d \propto E_i^k$ and we performed a least-square fit of the TRIM data (solid line in Fig. 3). The fitting is good and k turns out to be 0.5 and 0.6 for Xe and Ar, respectively.

Having established that an increase in E_i results in a larger d, we now argue how a larger d could result in bigger sized bubbles. In the subsurface region, the surface plays the role of the boundary of an infinitely sized void. So, a rg with a low E_i implanted close to the surface during the course of bombardment will be in a highly nonequilibrium situation and will undergo collision and diffusion processes. Being close to the surface, the probability for this ion to desorb out will be larger and so its chance to coalesce with a bubble and increase its size will be less as compared to a rg atom implanted deeper by a larger E_i. An evidence of rg desorption with increasing annealing temperature will be shown latter. Thus, the rg atom with a larger d, although still in the subsurface region, will have a higher chance of vacancy absorption and coalescence, resulting in a larger bubble size. Thus, R is an increasing function of E_i, since E_i increases d and, in turn, d increases R.

The above discussion implies that the concentration of a rg will be higher for a larger E_i, since for a larger d, the probability of the rg atom escaping through the surface decreases. To test this, we have determined the rg concentration in a region of 150 Å from the Al surface. This is the maximum depth to which Ar or Xe would be implanted as per our TRIM calculations. To determine the concentration, we find the areas under the respective Xe $3d_{5/2}$ (or Ar $2p$) and Al $2p$ core level peaks from the least-square fitting.

The Al $2p$ intensity (I_{Al}) can be expressed as

$$I_{\mathrm{Al}} = \sigma_{\mathrm{Al}\,2p} T \int_0^\infty N_{\mathrm{Al}}(x) \exp(-x/\lambda_{\mathrm{Al}}) dx, \tag{3}$$

where $\sigma_{\mathrm{Al}\,2p}$ is the photoemission cross section of Al $2p$, T is the analyzer related constant including an analyzer transmission function and étendu, and N_{Al} is the Al atom density at x, where x is the perpendicular distance from the surface at $x=0$.[29] Since Al is uniformly distributed, N_{Al} is a constant. Thus, $I_{\mathrm{Al}} = \sigma T N_{\mathrm{Al}} \lambda_{\mathrm{Al}} \Rightarrow N_{\mathrm{Al}} = I_{\mathrm{Al}} / \sigma T \lambda_{\mathrm{Al}}$. For a slab of thickness 150 Å, the total number of Al atoms is proportional to $N_{0\,\mathrm{Al}} = 150 N_{\mathrm{Al}}$.

The rg core level intensity (I_{rg}) can be written as

$$I_{rg} = \sigma_{rg} T \int_0^\infty N_{rg}(x) \exp(-x/\lambda_{rg}) dx, \tag{4}$$

where σ_{rg} is the photoemission cross section for the particular rg core level and $N_{rg}(x)$ is the rg atom density at x. Note that unlike Al density, $N_{rg}(x)$ is x dependent. This was not considered in Ref. 8. The rg distribution is approximately triangular and centered around d, which increases with E_i (Fig. 3). Hence, we take $N_{rg}(x) = N_{0rg} f(x)$, where N_{0rg} is a constant and $f(x)$ represents a symmetric triangular distribution of unit area centered around d. The value of d is obtained from the TRIM calculation discussed earlier. $f(x)$ is nonzero between $d-w \leqslant x \leqslant d+w$. The height ($h$) and FWHM ($w$) are related by $h = 1/w$. The total number of implanted rg atoms is given by $\int_0^\infty N_{0rg} f(x) dx = N_{0rg}$, since $\int_0^\infty f(x) dx = 1$. From Eq. (4),

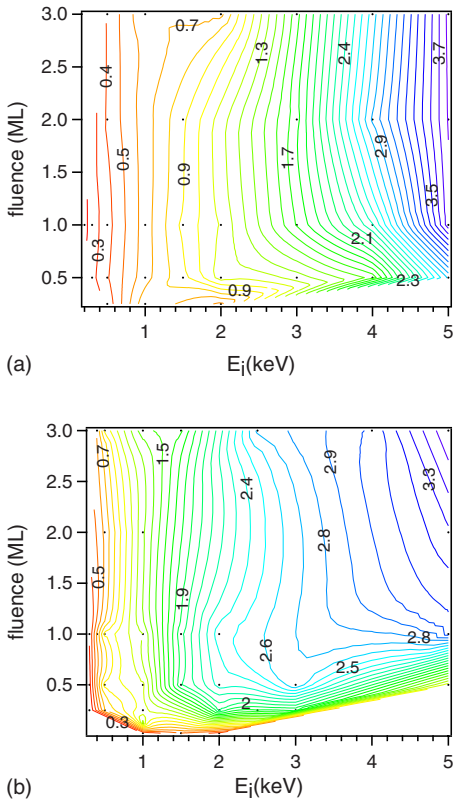

FIG. 4. (Color online) Variation in the percentage concentration (c) of (a) Xe in Al [in gray scale (rainbow for color): the darkest (blue) contour, 3.8%; the lightest (red) contour, 0.17%] and (b) Ar in Al [in gray scale (rainbow for color): the darkest (blue) contour, 3.6%; the lightest (red) contour, 0.2%] as a function of ion implantation energy and fluence.

$$N_{0rg} = I_{rg} / \sigma_{rg} T A. \tag{5}$$

To find N_{0rg}, we have solved the integral A as follows:

$$A = \int_0^\infty f(x) \exp(-x/\lambda_{rg}) dx \tag{6a}$$

$$= \exp\left(\frac{-d}{\lambda_{rg}}\right)\left(1 + \frac{1}{12}\frac{w^2}{\lambda_{rg}^2} + \frac{1}{360}\frac{w^4}{\lambda_{rg}^4} + \frac{1}{20160}\frac{w^6}{\lambda_{rg}^6}\right). \tag{6b}$$

The percentage concentration (c), as shown in Fig. 4, is thus given by

$$c = \left(\frac{N_{0rg}}{N_{0rg} + N_{0\mathrm{Al}}}\right) \times 100. \tag{7}$$

Figure 4(a) shows the Xe concentration and, indeed, we find that the concentration increases with E_i. The Concentration of Xe is about 0.3% at smallest E_i, increases to 1% at 2 keV, and almost becomes 4% at 5 keV. Ar also exhibits a similar increase in concentration with E_i [Fig. 4(b)]. In both cases, the increasing trend is observed almost independent of fluence. Thus, our proposition that a larger E_i results in a

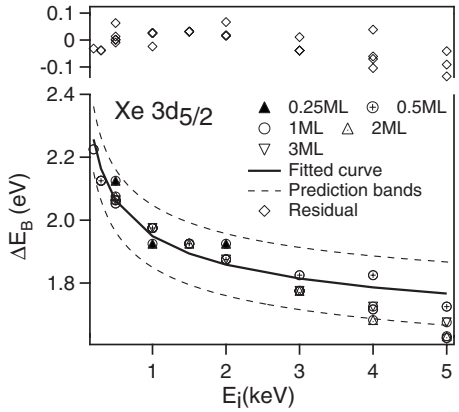

FIG. 5. ΔE_B variation for Xe $3d_{5/2}$ as a function of E_i for different fluences with fitted curve (solid line) and 90% prediction bands (dashed lines). The residual is shown at the top.

larger concentration and, hence, larger R is supported by Fig. 4.

Another argument to directly relate R with E_i is based on scanning tunneling microscopy (STM) experiments, which have shown that adatoms and voids in an Al substrate are produced by low doses of rg ion bombardment using 0.3–1 keV ion energy.[30] According to Ref. 30, adatom layers form because locally melted metal flows out to the surface due to the thermal spike created by the incident rg ions. From Fig. 4 of Ref. 30, it is clear that the volume of the void left behind will be equal to the volume that the adatoms would have occupied. It is shown that the number of adatoms formed due to one impact (hence void volume) is proportional to the melt volume. The melt volume is, in turn, proportional to E_{nuc}, which is the energy available for nuclear collisions [from Eq. (1) of Ref. 30]. Thus, the volume of the voids where rg atoms could be trapped to form bubbles is proportional to E_{nuc}. These rg filled voids are the bubbles whose radius R will then be proportional to $E_{nuc}^{1/3}$. In this low ion implantation energy range of a few keV's, the nuclear stopping power dominates the electronic stopping power and so E_i is almost equal to E_{nuc} (E_{nuc} is about 90% of E_i from TRIM calculation for both Xe and Ar). Thus, it can be qualitatively argued that R is proportional to $E_i^{1/3}$, so that we can arrive at a model function that will describe the ΔE_B variation with E_i.

On the basis of the above discussion and following Ref. 8, we use an expression $R=c_3E_i^n$, where c_3 is a proportionality constant and n determines the rate of increase of R (Å) with E_i (keV). By using this expression for R in Eq. (2), we obtain

$$\Delta E_B = \Delta E_R + c_2 = \frac{c_1}{c_3 E_i^n} + c_2 = \frac{c_1'}{E_i^n} + c_2. \tag{8}$$

We have been able to explain the BE variation and determine the bubble radius for Ar by using the above expression in Ref. 8. Here, we use Eq. (8) to fit the experimental data for Xe (Fig. 5) to examine whether a similar explanation is also valid for Xe. Since, as discussed earlier, there is a small change in ΔE_B with a fluence above 0.025 ML, we have considered the data for different fluences for a particular E_i. This shows that, independent of the fluence, ΔE_B decreases with E_i. A similar approach was followed for Ar bubbles in Al.[8] For Ar $2p$, the constant term c_2 turns out to be 1.4 ± 0.02 eV, which can be identified to be the asymptotic value approaching $E_i=3$ keV, where the c_1'/E_i^n term becomes small. This is expected because for larger sized bubbles, the effect of an extra atomic screening by Al conduction electrons would be smaller. However, for very large bubbles, other mechanisms, such as a phase transition from a solid to a liquid and a gaseous state due to a decrease in pressure, change of intrabubble screening, dipole term, etc., will dominate. This is because ultimately for very large bubbles where Xe or Ar is in a gaseous phase, ΔE_B should be zero.

For Xe bubbles, it is clear that the overall change of ΔE_B is smaller (0.6 eV) than that of Ar (1.1 eV). On this basis, it can be argued that the increase in Xe bubble size will be smaller than Ar in the studied E_i range. For fitting ΔE_B of Xe $3d_{5/2}$ (Fig. 5), we constrain the asymptotic constant c_2 to be between 1.5 and 1.7 eV (for Ar, $c_2=1.4$ eV) to avoid spurious unphysical results. The fit is rather good, which validates our explanation, as shown by the prediction band that gives the certainty of the scatter about a certain regression line. A 90% prediction band (Fig. 5) should have 90% of the data points contained within the bands, which is, indeed, so in this case. The value of n turns out to be 0.32 ± 0.1 for Xe, which is smaller than n (=0.5) for Ar, indicating a smaller variation of R for Xe.

Following Ref. 8, we presume that for a very low E_i where the rg concentration is small, the atoms are isolated as single atom implants in Al. This is justified since the experimental value of ΔE_B for Xe atoms implanted in Cu and Au are 2.17 and 2.41 eV,[12] respectively, which are close to $\Delta E_B=2.25$ eV at the lowest $E_i=0.2$ keV for Xe in Al. So, for $E_i=0.2$ keV, if R is equal to the van der Waals radius (R_o) of a single rg atom (which are 2.16 and 1.88 Å for Xe and Ar, respectively[31]), we can calculate R for higher E_i by R (say, at 5 keV)$=(5/0.2)^n R_o$. Thus, we provide an approximate estimate of the Xe bubble radius of 6 Å, while the Ar bubble radius is 9 Å at 5 keV. To the best of our knowledge, there is no reported value of R for Xe bubbles in the 0–5 keV range; however, for higher E_i, R is reported to be about 17 Å at 50 keV[3], and 10 Å at 35 keV.[6,32] Thus, R estimated by us at 5 keV is in agreement with the trend in R for higher E_i.

B. Binding energy shift with fluence and concentration

Having discussed the BE change with E_i, we now turn to the discussion of BE shift with fluence. For higher E_i, ΔE_B for Xe decreases slightly with fluence from 1.83 eV (0.5 ML), 1.78 eV (1 ML), and 1.73 eV (3 ML) for $E_i=4$ keV. To examine the effect of a much larger fluence, Xe $3d$ and Ar $2p$ core level spectra for 10 ML fluence have been recorded at $E_i=2$ keV; however, hardly any change of BE is observed between 3 and 10 ML. For $E_i=0.5$ keV, ΔE_B is 2.43, 2.13, 2.06, 2.05, 2.08, and 2.06 for 0.025, 0.25, 0.5, 1, 2, and 3 ML, respectively. Thus, as in Ar $2p$, ΔE_B exhibits some variation at small fluence and then stabilizes for higher fluence above 0.5–1 ML. This is related to an initial increase

in rg concentration with fluence, as is also shown in the concentration plots in Fig. 4. An increase in concentration implies larger probability of coalescence, leading to bubble growth.

However, from Fig. 2, it is obvious that the change in ΔE_B with fluence is not as pronounced as that with E_i. Although this may seem to be counterintuitive, we emphasize that fluence gives the number of rg ions incident on the surface, which is not necessarily the same as the concentration of the actually implanted rg atoms. In fact, this is clearly shown in Fig. 4. For both Xe and Ar, the concentration hardly varies with fluence above 0.5–1 ML. A dynamic equilibrium between the rg implantation and the backscattering processes, including a sputtering out of the already implanted rg atoms in the subsurface region, could be a reason for this. The concentration plots in Fig. 4 explain the absence of ΔE_B variation with fluence (Fig. 2).

C. Effect of pressure on binding energy

Ar and Xe bubbles in Al are reported to be in the solid phase at room temperature due to the large pressure exerted by the Al lattice up to about 30–60 kbars.[1,33] Faraci *et al.*[33] estimated the pressure to be 25 kbars from the nearest neighbor Ar-Ar distances for Ar bubbles in Al by extended x-ray absorption spectroscopy. The shift in He 1^1S_0-2^1P_1 transition line for He bubbles in Al under different implantation conditions have been found to be proportional to the density of the He bubbles and, thus, related to pressure.[1] With increasing size of the bubble, the pressure (p) decreases: $p=2\gamma/R$, where γ is the surface tension of the bubble. A decrease of pressure decompresses the rg wave functions and modifies the Coulomb interaction, resulting in a change in the energy of the initial state causing BE shift. In order to study this effect on the inner shell core level excitations (such as Ar $2p$) and on outer shell shallow core levels (such as Ar $3p$), we have performed calculations for bulk solid Ar by using an *ab initio* full potential linear augmented plane wave (FPLAPW) method employing the WIEN97 code.[34] Note that the FPLAPW calculation does not consider the full system, i.e., the metal matrix that has embedded Ar bubbles. The reason for performing FPLAPW calculations is as follows: the BE energy shift can be explained by the change in screening (a final state effect) or by the change in pressure (initial state effect). Both effects are described in the literature to vary as $1/R$.[8] The present calculations help us to eliminate or include the possible influence of the initial state pressure effect on the observed BE shift.

Solid Ar has a fcc structure with a $Fm3m$ space group and a lattice constant $a=5.26$ Å.[35] Finger *et al.*[36] have studied solid Ar by x-ray diffraction as a function of pressure. They found that above 11.5 kbar, Ar is in a solid phase at 293 K and a decreases as pressure is increased (inset of Fig. 6, based on Table I of Ref. 36). Since the lattice contracts with the application of pressure, we have done the calculations by decreasing the lattice constant by step of 2% from $a=5.26$ Å to $a=4.63$ Å to simulate the reported pressure up to 60 kbars on Ar bubbles.[1] The change in BE of Ar $2p$ and $3p$ core levels with decreasing lattice constant (or increasing pressure) starting from $a=5.26$ Å (at normal pressure) is shown in Fig. 6.

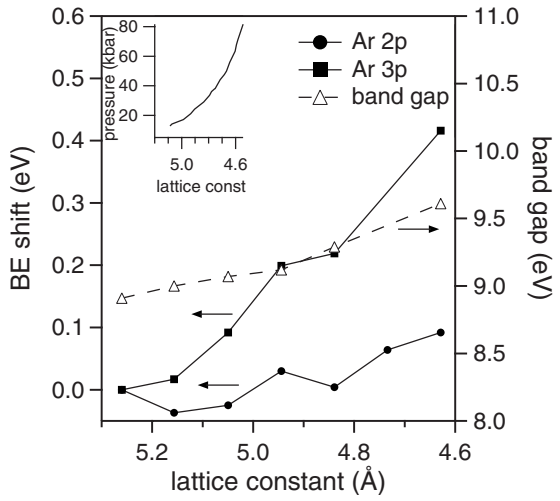

FIG. 6. The increase in BE of Ar $2p$ (filled circles) and $3p$ (filled squares) core-level spectra with decreasing lattice constant for bulk solid Ar. The variation of pressure with lattice constant from Ref. 36 is shown in the inset. Zero corresponds to the BE value at normal pressure. The change in band gap is also shown.

Figure 6 clearly shows that while Ar $3p$ BE increases monotonically to more than 0.4 eV, the BE of Ar $2p$ oscillates around zero until 4.8 Å, after which it shows a small increase to 0.09 eV at 4.6 Å, which corresponds to about 60 kbar pressure. This shows that the explanation for the experimentally observed large BE shift of about 1.1 eV for Ar $2p$ [Fig. 2(b)] cannot be explained by the change in pressure. The insensitivity of Ar $2p$ to pressure as compared to Ar $3p$ is because the former is a deep core level with a localized atomic wave function. So, it is not affected by external pressure. Ar $3p$ shows a shift as a function of pressure because it is a shallow core level with an extended wave function that is readily compressed by increasing pressure. A similar effect is observed in the He 1^1S_0-2^1P_1 transition, where the excited state $2P$ wave function is four times larger than the $1S$ ground state.[1]

The Ar $3p$ shallow core level and the XPS valence band spectra are shown in Fig. 7 for different E_i's. The free-electron-like parabolic spectral shape with the Fermi level at zero of the energy scale represents the Al valence band. A broad peak appearing at 9.4 eV ($E_i=0.3$ keV) corresponds to the Ar $3p$ core level. In the gas phase, the BE's (referred to as the vacuum level) of Ar $3p_{3/2}$ and $3p_{1/2}$ are 15.9 and 15.7 eV, respectively.[23] The BE of Ar $3p$ is 13.6 eV at $E_i=0.3$ keV with respect to the vacuum level of Al. Thus, there is a shift of about 2.3 eV from the gas phase BE, as in the case of Ar $2p$. With E_i increasing from 0.3 to 3 keV, a gradual increase in BE from 9.4 to 10.2 eV is observed. So, the overall shift is 0.8 eV, which is higher than the 0.6 eV shift observed in the same E_i range for Ar $2p$. To conclude, the BE increase for a shallow core level such as Ar $3p$ can be ascribed to a combined final state effect of decreased screening and initial state effect of decreased pressure with the increase in the bubble size.

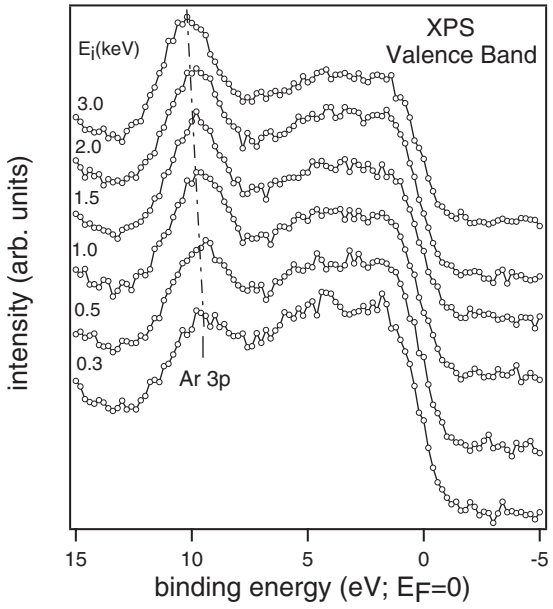

FIG. 7. XPS valence band showing the Ar $3p$ core-level spectra of Ar bubbles in Al for different E_i's. The Fermi energy is indicated by E_F (at 0 eV). The shift of the Ar $3p$ peak is shown by a dot-dashed line.

It is noteworthy that the existence of high pressure on the Xe bubbles in Al has, in fact, been questioned by the work of Donnelly and Rossouw.[3] For solid Xe bubbles in Al, a pressure of 7 kbars is reported, which is smaller than the equilibrium pressure of 11 kbars.[3] This is also evident from the absence of any strain contrast around the bubbles in the TEM image. Birtcher *et al.* have shown that when solid Xe bubbles coalesce, rather than the total area, the total volume remains conserved. This implies that the pressure is not determined solely by the interface tension, in contrast to He bubbles, where the surface area is conserved upon coalescence and $p=2\gamma/R$ is followed.[6] Thus, the pressure need not be inversely proportional to the bubble radius in Xe. Moreover, even if there is some change in pressure with R, Xe $3d$, being a deeper core level than Ar $2p$, will be unaffected.

D. Variation of rare gas core-level line shape

From Fig. 1, an obvious change in the line shape is in the FWHM, which increases with E_i. This is an extra Gaussian broadening that had to be introduced in the fitting scheme even after considering the instrumental resolution broadening. We show the variation of the FWHM of the Gaussian (w_g) with implantation conditions as contour plots in Fig. 8, for both Xe $3d_{5/2}$ and Ar $2p$. For the Xe $3d_{5/2}$ spectra, w_g increases from 0.3 eV for E_i=0.2 keV to 0.8 eV for 5 keV [Fig. 8(a)]. For Ar $2p$, we observe an even more pronounced broadening of 0.4 eV at E_i=0.3 keV that increases to 1.3 eV at 5 keV. We find that w_g increases with E_i, while there is not much change with fluence. To understand the origin of this broadening, we note that there is always a distribution of the bubble size around the mean R. For example, Donnelly and Rossouw[3] reported a roughly symmetrical distribution of Xe

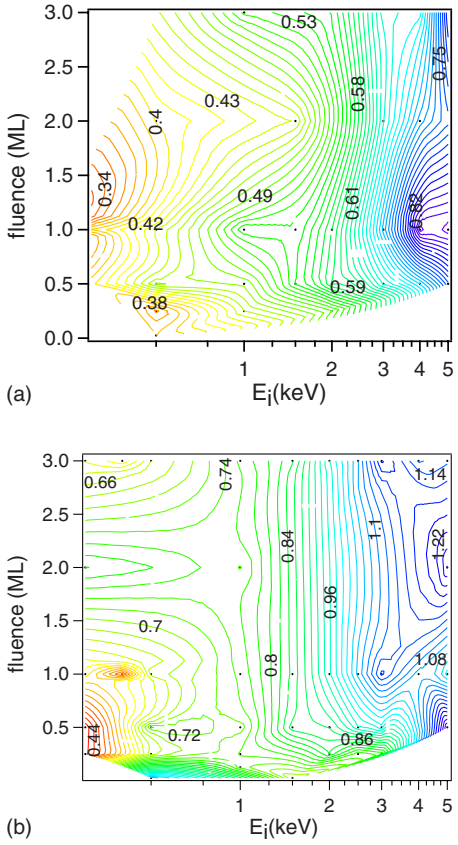

FIG. 8. (Color online) (a) Variation in the FWHM (w_g) of the Gaussian broadening for Xe $3d_{5/2}$ as function of E_i and F. In gray scale (rainbow for color), the darkest (blue) contour corresponds to 0.87 eV and the lightest (red) contour to 0.29 eV. (b) Variation of w_g for Ar $2p$, where in gray scale (rainbow for color), the darkest (blue) contour corresponds to 1.3 eV and the lightest (red) contour to 0.4 eV.

bubbles in Al with the mean R of 17 Å and a standard deviation of 5 Å. Since the BE of the rg core level depends on the bubble size, a symmetrical distribution of bubble size will result in a symmetrical distribution of the core level peak position around the mean position, corresponding to the mean R. This implies that higher the FWHM of the size distribution, larger the w_g. If this proposition is correct, the FWHM should be higher for Ar, since w_g is larger in Ar as compared to Xe. Since d is related to R, this is indeed so, as shown by a larger FWHM of the depth distribution for Ar from the TRIM calculation [inset of Fig. 3(b)]. In fact, the FWHM of the depth distribution for Ar is about twice that of Xe (insets in Fig. 3), which is in the order of the ratio of w_g for Ar and Xe. Another factor that might contribute to the extra width of the bubbles is the location of the photoemitting rg atom within the bubble, since, depending on whether the photohole is located centrally or near the bubble surface, the relaxation energy might change, giving rise to a small difference in BE.

The well known asymmetric line shape of metal core levels toward the higher BE side is known as the Doniach–Šunjić asymmetry.[18] This asymmetry is quantified by the asymmetry parameter α and, in literature, α for Al metal has

been reported to be 0.11.[21,22] The asymmetry is related to the infinitesimal electron-hole excitations across the Fermi level due to the scattering of the conduction electrons by a sudden creation of the core hole in the final state of photoemission. This asymmetry is absent in insulators for the obvious reason that there is no Fermi level. So, indeed, for bulk solid Ar, which is a high band gap insulator (the calculated band gap and its variation with pressure are shown in Fig. 6), α should be zero. However, the situation in solid nanometer sized bubbles surrounded by Al is completely different from bulk solid rg. Here, the sea of conduction electrons at the Al Fermi level will be perturbed by the core-hole formation in the bubble and undergo electron-hole excitations, causing an asymmetry in the Ar $2p$ core level.

For both Ar $2p$ and Xe $3d_{5/2}$, we find the trend that for low E_i, where R is small, α is significantly different from zero. Interestingly, for large E_i, the line shape becomes symmetric with $\alpha \rightarrow 0$. This has been shown in detail for Ar $2p$ in Ref. 8. Here, we extend the data up to E_i=5 keV and find α=0.008 for Ar $2p$. A similar trend for Xe $3d_{5/2}$ has been observed. Thus, it is the final state screening of the rg core hole that changes with R and causes a shift in the BE and a change in the line shape of the deep core levels. Finally, an interesting point to be noted is that α, i.e., the asymmetry, decreases as fluence and E_i increase. On the other hand, if it is assumed that the asymmetry was caused by different rg defect complexes, as for Ne in Cu, where bubble formation is not reported,[12] the asymmetry would have increased as fluence and E_i increased. This is obvious because as the implantation conditions become harsher due to increased E_i and fluence, the number of such defect complexes and the asymmetry will increase.[12] This does not happen for a rg in Al, which demonstrates that most of the implanted rg atoms precipitate into bubbles.

E. Effect of high temperature annealing on rare gas core level binding energy

The growth of rg bubbles in Al due to high temperature annealing has been studied in literature.[37–41] From the shift of the He $1^1S_0-2^1P_1$ transition line, Manzke *et al.*[37] concluded that above 473 K, the He bubble density decreases due to the increase in bubble size. Rajainmäki *et al.*[39] showed that above 600 K, He bubbles grow by bubble coalescence and condensation of thermally produced vacancies. For higher annealing temperatures, the concentration would decrease, as most of the bubbles would move to the surface and desorb.[1] Our recent positron annihilation spectroscopy studies on Al implanted with 130 keV Ar^+ show that the bubble size increases with annealing.[41]

Figure 9(a) shows the decrease in ΔE_B (or increase in BE) of Ar $2p$ core level spectra for bubbles formed with E_i =1.5 keV and 1 ML fluence, which have been annealed at different temperatures for 3 min. The data are recorded subsequently at room temperature. For each annealing temperature (T_A), a fresh implantation has been performed. However, for the 200 K data, both implantation and data collection have been performed at 200 K. Between 200 and 540 K, ΔE_B decreases by about 0.2 eV [Fig. 9(a)]. The core level

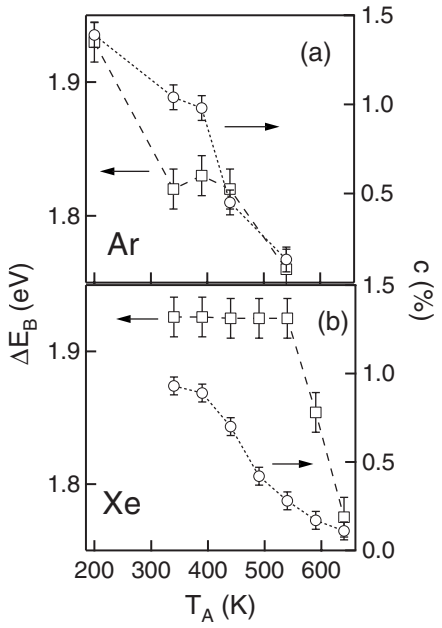

FIG. 9. ΔE_B (square) and concentration (c, circle) of (a) Ar $2p$ and (b) Xe $3d_{5/2}$ core level spectra as a function of annealing temperature (T_A). The arrows indicate the axes.

peak positions have been determined by least-square fitting, as discussed in Sec. II. An increase in BE of about 0.1 eV between 200 and 340 K shows that at the lower temperature, the bubble size is smaller. Between 340 and 440 K, the BE does not change much, while at higher temperatures, it clearly increases. The Xe $3d_{5/2}$ spectra also exhibit a similar trend of decrease in ΔE_B as a function of T_A. ΔE_B decreases from 1.92 to 1.78 eV, i.e., an overall BE shift of about 0.15 eV [Fig. 9(b)]. No extra feature appears in the annealed rg core level spectra.

As discussed earlier, the increase in size of a rg bubble with annealing is well known in literature for He and has been related to a higher mobility of the rg atom at higher temperature.[1,37] A proof of enhanced mobility of Ar and Xe atoms is obtained from the decrease in concentration (c) with increasing T_A (Fig. 9). c has been calculated by using Eqs. (3)–(7). c for Ar decreases from 1.4% at 200 K to less than 0.2% at 540 K. Similarly, for Xe, c dereases from about 0.9% to 0.1% between 340 and 640 K. No XPS signal corresponding to the rg atom is detected for annealing at 723 K, which is used by us to regenerate the rg free ordered Al(111) surface before each implantation (see Sec. II). For the subsurface bubbles studied here, the decrease in concentration is drastic as compared to bubbles implanted in the bulk using $E_i \geqslant 50$ keV, where even up to the Al melting point, a finite rg concentration is observed.[38,41]

Since the rg ions are implanted in the subsurface region, an increase in mobility with increasing temperature results in more rg atoms reaching the surface with enough energy to desorb. Thus, a decrease in c would result from a higher mobility of the rg atoms, which, in turn, would result in a larger bubble size. Thus, c shows a decreasing trend as ΔE_B. Note that for Xe, c starts decreasing from 400 K, while ΔE_B decreases only above 540 K. In contrast, for Ar, c and ΔE_B

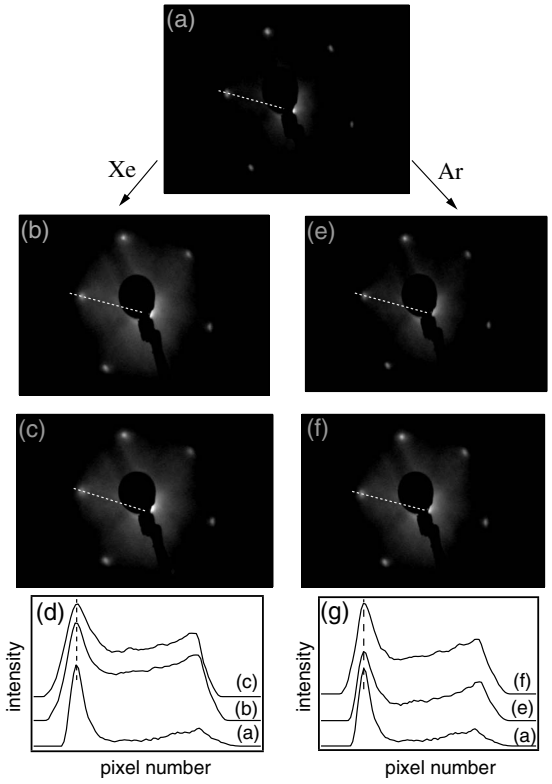

FIG. 10. LEED pattern recorded with 112 eV electron beam energy for (a) a clean Al(111) surface as compared to xenon implanted Al(111) with (b) 0.5 keV and (c) 5 keV, and argon implanted Al(111) with (e) 0.5 keV and (f) 5 keV. Here, all the implantations are for a fluence of 3 ML. The intensity profiles along the dashed white line are shown for Xe and Ar implantations in (d) and (g), respectively.

exhibit a similar variation. The reason is related to the details of the mechanism of bubble growth in rg with annealing, and microscopic studies using TEM or STM may be necessary to understand this.

The increase in BE as T_A increases further supports our contention that, indeed, the BE shift observed with implantation conditions is related to the size of the rg bubbles. For Xe (Ar), a substantial decrease in ΔE_B as compared to near room temperature data (340 K) occurs above 540 K (400 K). A decrease in ΔE_B implies an increase in bubble size, as discussed earlier (Fig. 5). This observation is in agreement with the result for He bubbles, where bubble growth was observed above 473 K.[37] Thus, bubble growth occurs at a higher temperature for Xe, which is understandable since Xe is heavier and would require a higher thermal energy for mobility.

F. Effect of rare gas implantation on the Al(111) surface

The clean and implanted Al(111) surfaces have been studied by LEED to ascertain the extent of surface disorder induced by rg bombardment (Fig. 10). The LEED pattern for clean Al [Fig. 10(a)] shows the characteristic pattern for the (111) oriented surface of a fcc structure. Note worthy is the sharpness of the spots and low background signal, implying very good surface crystallinity. On the other hand, for the rg implanted surfaces, the background of the LEED pattern is clearly enhanced and the LEED spots are broader. This is shown quantitatively by the intensities along the white dashed line in Figs. 10(d) and 10(g) for Xe and Ar, respectively. These changes in the LEED pattern indicate the formation of defects on the Al(111) surface, which are disordered. The formation of random steps and terraces on the Al(111) surface by low energy rg ion bombardment has been reported by Busse *et al.*[30] For a predominantly rough surface, the spot profile broadens with enhanced background intensity.[42] Such a geometrical disorder on the surface weakens $\vec{k}_{\parallel}$ (wave vector parallel to the surface) conservation, resulting in a reduced coherence length and a broadening of LEED spots. Thus, defect induced partial disorder is observed due to rg bombardment.

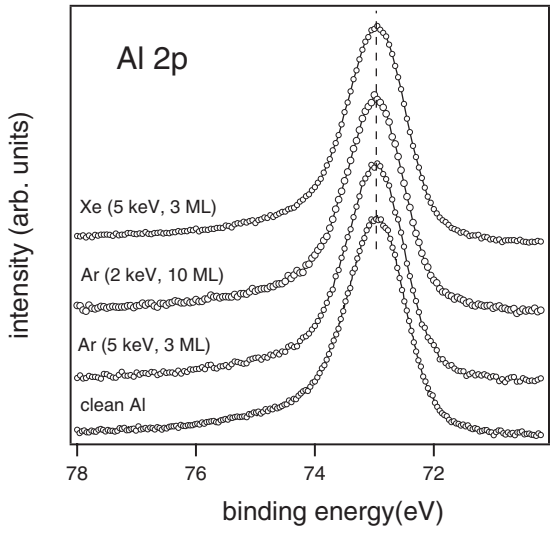

FIG. 11. Al $2p$ spectra for different implantation conditions of Xe and Ar (as indicated in brackets for each spectrum) compared to from clean Al without any implantation.

The changes in the Al(111) LEED prompted us to study the Al $2p$ core level spectra in detail. In Fig. 11, an Al $2p$ core level spectrum for the clean surface (i.e., after surface cleaning and before implantation) is compared to the extreme (highest E_i and fluence) implantation conditions for Xe and Ar. Interestingly, although the rg core levels sensitively change in BE and shape with E_i and fluence, the Al $2p$ spectra do not exhibit any change. This is in spite of the fact that a high signal to noise ratio of the data enables the detection of a small core level shift or change in line shape. In fact, for all implantation conditions, the Al $2p$ remains unaffected, as highlighted in Fig. 11 by the absence of any change between clean and harsh implantation conditions such as 5 keV and 10 ML. The insensitivity of Al $2p$ to implantation conditions ensures the following: (i) There is no charge transfer between the rg atoms and Al, and (ii) surface disorder or defects do not influence the XPS core level position and line shape.

IV. CONCLUSION

X-ray photoemission spectroscopy has been used to study the deep and shallow core levels of Xe and Ar rare gas

nanobubbles in Al. For both Xe $3d_{5/2}$ and Ar $2p$, we find a shift in the BE as a function of E_i and fluence. We find the behavior of Xe and Ar bubbles to be quite similar. An increase in BE (or a decrease in ΔE_B) with E_i has been related to the increase in bubble size, which decreases the Al conduction electron screening strength. The BE variation is pronounced with E_i, while the variation is less with fluence. This is explained by the actual concentration of rg in Al. The Doniach–Šunjić asymmetry of the rg core levels decreases with increasing bubble size, which further supports this explanation. The Xe bubble radius is estimated to be 6 Å at 5 keV, which is smaller than that of Ar (9 Å). By using density functional theory, we discard the explanation that a change in pressure can cause a BE shift in the inner shell core levels such as Ar $2p$ or Xe $3d$. On the other hand, for outer shell core levels, a pressure change would influence the BE, as in case of Ar $3p$. The extra Gaussian broadening of the core levels arises from the distribution of bubble size and is more pronounced in Ar $2p$ as compared to Xe $3d$. The change in BE of both Ar $2p$ and Xe $3d$ core levels has been studied by annealing them at high temperatures after implantation. The decrease in concentration with higher annealing temperature is related to the desorption facilitated by increased mobility of the rg atoms. The increase in binding energy with higher annealing temperature shows that the bubble size increases, which is consistent with the increase in mobility. Low energy electron diffraction studies show that defects introduced a partial disorder on the Al(111) surface. However, the absence of any change in the Al $2p$ spectra for different implantation conditions shows that this does not affect the core level position and line shape.

ACKNOWLEDGMENTS

We gratefully acknowledge useful discussions with J. Fink and G. Amarendra. S. D'Souza is thanked for help in data analysis. P. Chaddah, A. Gupta, V. C. Sahni, and S. M. Oak are thanked for encouragement. Fundings from Max-Planck-D.S.T. Partner Group project and Ramanna Research Grant are acknowledged.

*barman@csr.ernet.in

[1] J. Fink, Adv. Electron. Electron Phys. **75**, 121 (1989).
[2] A. vom Felde, J. Fink, T. Muller-Heinzerling, J. Pfluger, B. Scheerer, G. Linker, and D. Kaletta, Phys. Rev. Lett. **53**, 922 (1984).
[3] S. E. Donnelly and C. J. Rossouw, Science **230**, 1272 (1985); Nucl. Instrum. Methods Phys. Res. B **13**, 485 (1986).
[4] C. J. Rossouw and S. E. Donnelly, Phys. Rev. Lett. **55**, 2960 (1985).
[5] M. Schmid, W. Hebenstreit, P. Varga, and S. Crampin, Phys. Rev. Lett. **76**, 2298 (1996).
[6] R. C. Birtcher, S. E. Donnelly, M. Song, K. Furuya, K. Mitsuishi, and C. W. Allen, Phys. Rev. Lett. **83**, 1617 (1999).
[7] S. E. Donnelly, R. C. Birtcher, C. W. Allen, I. Morrison, K. Furuya, M. Song, K. Mitsuishi, and U. Dahmen, Science **296**, 507 (2002).
[8] C. Biswas, A. K. Shukla, S. Banik, S. R. Barman, and Aparna Chakrabarti, Phys. Rev. Lett. **92**, 115506 (2004).
[9] E. Arzt, O. Kraft, W. D. Nix, and J. E. Sanchez, Jr., J. Appl. Phys. **76**, 1563 (1994).
[10] K. Y. Chen and J. R. Cost, J. Nucl. Mater. **52**, 59 (1974).
[11] J. E. Inglesfield and J. B. Pendry, Philos. Mag. **34**, 205 (1976).
[12] P. H. Citrin and D. R. Hamann, Phys. Rev. B **10**, 4948 (1974); Chem. Phys. Lett. **22**, 301 (1973).
[13] R. E. Watson, J. F. Herbst, and J. W. Willkins, Phys. Rev. B **14**, 18 (1976).
[14] B. J. Waclawski, J. W. Gadzuk, and J. F. Herbst, Phys. Rev. Lett. **41**, 583 (1978).
[15] M. Abbate, Phys. Rev. B **39**, 7641 (1989).
[16] G. Kaindl, T. C. Chiang, D. E. Eastman, and F. J. Himpsel, Phys. Rev. Lett. **45**, 1808 (1980); T.-C. Chiang, G. Kaindl, and T. Mandel, Phys. Rev. B **33**, 695 (1986).
[17] K. Horn, M. Scheffler, and A. M. Bradshaw, Phys. Rev. Lett. **41**, 822 (1978); K. Hermann, J. Noffke, and K. Horn, Phys. Rev. B **22**, 1022 (1980); T. Mandel, G. Kaindl, M. Domke, W. Fischer, and W. D. Schneider, Phys. Rev. Lett. **55**, 1638 (1985).
[18] S. Doniach and M. Šunjić, J. Phys. C **3**, 285 (1970).
[19] W. H. Press, S. A. Teukolsky, W. T. Vetterling, and V. P. Flannery, *Numerical Recipes in Fortran* (Cambridge University Press, Cambridge, England, 1992).
[20] M. Jurvansuu, A. Kivimäki, and S. Aksela, Phys. Rev. A **64**, 012502 (2001).
[21] W. Theis and K. Horn, Phys. Rev. B **47**, 16060 (1993).
[22] C. Biswas, A. K. Shukla, S. Banik, V. K. Ahire, and S. R. Barman, Phys. Rev. B **67**, 165416 (2003).
[23] M. Cardona and L. Ley, *Photoemission in Solids: General Principles* (Springer-Verlag, Berlin, 1978).
[24] G. W. Greenwood, A. J. E. Foreman, and D. E. Rimmer, J. Nucl. Mater. **4**, 305 (1959).
[25] D. J. Reed, Radiat. Eff. **31**, 129 (1977).
[26] J. F. Ziegler, Appl. Phys. Lett. **31**, 544 (1977).
[27] J. P. Biersack and L. Haggmark, Nucl. Instrum. Methods **174**, 257 (1980).
[28] J. Martan, Nucl. Instrum. Methods Phys. Res. B **2**, 202 (1984).
[29] D. Briggs and M. P. Seah, *Practical Surface Analysis by Auger and X-ray Photoelectron Spectroscopy* (Wiley, New York, 1990).
[30] C. Busse, H. Hansen, U. Linke, and T. Michely, Phys. Rev. Lett. **85**, 326 (2000).
[31] A. Bondi, J. Phys. Chem. **68**, 441 (1964).
[32] C. W. Allen, R. C. Birtcher, S. E. Donnelly, K. Furuya, N. Ishikawa, and M. Song, Appl. Phys. Lett. **74**, 2611 (1999).
[33] G. Faraci, S. La Rosa, A. R. Pennisi, S. Mobilio, and G. Tourillon, Phys. Rev. B **43**, 9962 (1991).
[34] P. Blaha, K. Schwartz, and J. Luitz, *WIEN97, A Full Potential Linearized Augmented Plane Wave Package for Calculating Crystal Properties* (Techn. Universität, Wien, Austria, 1999).
[35] D. G. Henshaw, Phys. Rev. **111**, 1470 (1958).
[36] L. W. Finger, R. M. Hazen, G. Zou, H. K. Mao, and P. M. Bell, Appl. Phys. Lett. **39**, 892 (1981).

[37] R. Manzke, G. Crecelius, W. Jager, H. Trinkaus, and R. Zeller, Radiat. Eff. **78**, 327 (1983).
[38] H. E. Hansen, H. Rajainäki, R. Talja, M. D. Bentzon, R. M. Nieminen, and K. Petersen, J. Phys. F: Met. Phys. **15**, 1 (1985).
[39] H. Rajainmäki, S. Linderoth, H. E. Hansen, R. M. Nieminen, and M. D. Bentzon, Phys. Rev. B **38**, 1087 (1988).
[40] K. O. Jensen, M. Eldrup, B. N. Singh, and M. Victoria, J. Phys. F: Met. Phys. **18**, 1069 (1988).
[41] R. S. Dhaka, K. Gururaj, S. Abhaya, S. Amirthapandian, B. K. Panigrahi, K. G. M. Nair, G. Amarendra, and S. R. Barman, Proceedings of DAE Solid State Physics Symposium, Mysore (2007), Vol. 52, p. 659.
[42] M. A. Van Hove, W. H. Weinberg, and C.-M. Chan, *Low-Energy Electron Diffraction* (Springer-Verlag, Berlin, 1986).